Review of Scientific Instruments

Load sensitive stable current source for complex precision pulsed electroplating

Cite as: Rev. Sci. Instrum. **90**, 104704 (2019); https://doi.org/10.1063/1.5113790
Submitted: 08 June 2019 . Accepted: 24 September 2019 . Published Online: 09 October 2019

Omar Nassar, Markus V. Meissner, Sagar Wadhwa, Jan G. Korvink, and Dario Mager

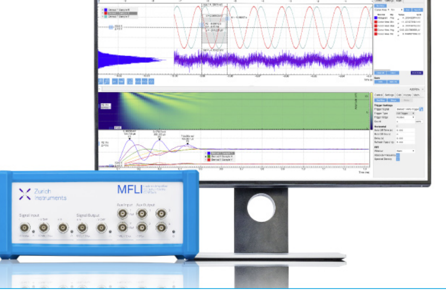

© 2019 Author(s).

Review of Scientific Instruments | ARTICLE | scitation.org/journal/rsi

Load sensitive stable current source for complex precision pulsed electroplating

Cite as: Rev. Sci. Instrum. 90, 104704 (2019); doi: 10.1063/1.5113790
Submitted: 8 June 2019 • Accepted: 24 September 2019 •
Published Online: 9 October 2019

Omar Nassar, Markus V. Meissner, Sagar Wadhwa, Jan G. Korvink,[a] and Dario Mager

AFFILIATIONS

Institute of Microstructure Technology, Karlsruhe Institute of Technology (KIT), Hermann-von-Helmholtz-Platz 1, 76344 Eggenstein-Leopoldshafen, Germany

[a]Author to whom correspondence should be addressed: jan.korvink@kit.edu

ABSTRACT

Electrodeposition is a highly versatile and well explored technology. However, it also depends strongly on the experience level of the operator. This experience includes the pretreatment of the sample, and the composition of the electrolyte settings of the plating parameters. Accurate control over the electroplating current is needed especially for the formation of small structures, where pulsed electrodeposition has proven to reduce many unwanted effects. To bring precision into the formation of optimal recipes, a highly flexible current source based on a microcontroller was developed. It allows a large variety of pulse waveforms, as well as maintaining a feedback loop that controls the current and monitors the output voltage, allowing for both galvanostatic (current driven) and potentiostatic (voltage driven) electrodeposition. The system has been implemented with multiple channels, permitting the simultaneous electrodeposition of multiple substrates in parallel. Being based on a microcomputer, the system can be programmed using predefined recipes individually for each channel, or even adapt the recipes during plating. All measurement values are continuously recorded for the purpose of documentation and diagnosis. The current source is based on a high power operational amplifier in a modified Howland current source configuration. This paper describes the functionality of the electrodeposition system, with a focus on the stability of the source current under different electrodeposition current densities and frequencies. The performance and high capability of the system is demonstrated by performing and analyzing two nontrivial plating applications.

© *2019 Author(s). All article content, except where otherwise noted, is licensed under a Creative Commons Attribution (CC BY) license (http://creativecommons.org/licenses/by/4.0/).* https://doi.org/10.1063/1.5113790

I. INTRODUCTION

Over the last two centuries, electrodeposition has repeatedly proven its ability to coat substrates with a large variety of materials. These include pure metals, metal composites, alloys, conductive polymers, semiconductors, and oxides.[1] Electrodeposition has been extensively investigated for its various applications and has had a significant impact on the materials sciences. Beyond the conventional applications of corrosion, erosion, and wear resilience,[2] electrodeposition has been used in highly advanced applications, from micro- and nanofabrication,[3,4] as well as integrated circuits (ICs),[5] all the way to large thick-walled (above millimeter) electroformed products.[1,2] Electrodeposition has many advantages, which make it one of the most used fabrication processes in research and industry, including low cost, purity, rapidity, freedom from porosity, industrial capability, ability to coat different substrates, producing structures in the range of micrometer to nanometer, and controlled alloy composition.[6,7]

Electrodeposition processes involve several parameters which can be manipulated, such as electrolyte bath composition, *p*H value, temperature, current density, and additives. Varying any of the parameters leads to a change in the features of the deposited film, including crystallite size, texture, and embedded film stresses.[1] Controlling the current distributions through the electrolyte has a significant effect on the deposited film structure and can be controlled either by using additives or through pulsed electroplating.[1] For simplicity, and to obtain a reliable electrodeposited process, it is better to reduce or even avoid the usage of chemical additives.[8] Pulsed electroplating has been widely considered and investigated over the last years as it has the advantage of controlling the properties and features of the deposited film while reducing the need for additives.[1,9] Pulsed electrodeposition gives control over (i) grain

© Author(s) 2019

size and structure,[10–13] (ii) feature and roughness of the deposited layer,[1,14] (iii) ion distribution within the electrolyte avoiding high current density regions,[15–17] (iv) mechanical and physical properties of the deposited material,[18] (v) mass transport electrocrystallization,[10,19–22] (vi) porosity and hydrogen content,[23,24] and (vii) atomic and microscale structures.[8,25]

Pulsed electrodeposition has been considered in several publications, as well as in industrial fabrications. Western Electric in the 1970s[26] implemented the first significant application of pulsed plating by depositing gold for electronic switching crossover circuits. The electroplating time was reduced by 50% compared to using direct current (DC). The pulse timing settings were 0.1 ms ON and 0.9 ms OFF; these settings are still commonly used today for plating soft gold. Pulsed electroplating has been used as well in the field of optics, where bipolar pulsed electroplating was used for creating highly antireflective surfaces.[27]

Despite the advantage of pulsed electrodeposition, it still faces some challenges regarding its practicability. Generating current pulses, especially with complicated waveforms, is associated with more costly equipment than a normal DC unit;[15,28,29] hence, applications of the more sophisticated pulsed electroplating is rarely found in practice.

In this paper, an electroplating power source with very high functional capability is introduced, which can be used to develop complex galvanostatic and potentiostatic electrodeposition processes. The developed system was demonstrated on two applications: we studied and solved the challenges of electroplating inkjet printed conductive structures formed on unstructured and thin flexible Kapton substrates, and we performed an eightfold parallel electroplating step for a complex microfabrication MEMS process.

The remainder of the article has three sections: Section II discusses electroplating waveforms found in the literature;[15,29] Sec. III describes the design and characterization of the power source and its controller; and Sec. IV illustrates the capability of the devices for the two applications.

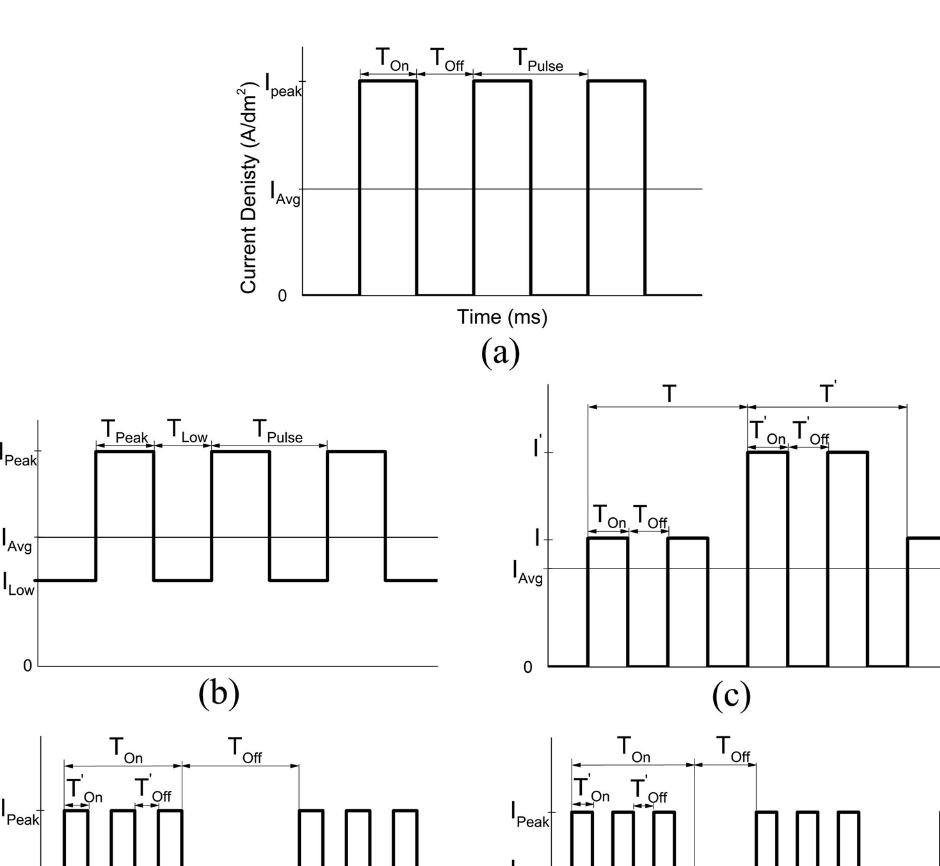

FIG. 1. Waveforms for unipolar pulsed electrodeposition: (a) pulse, (b) superimposed pulse, (c) duplex pulse, (d) pulsed pulse, and (e) pulse on pulse.

© Author(s) 2019

II. WAVEFORMS FOR PULSED ELECTRODEPOSITION

Several devices and tools have been patented and are available for generating waveforms for pulsed electrodeposition, as well as for pulsed anodization. The techniques range from manually switching a current for periods of a few minutes to using a microprocessor to achieve a programmable current source.[30] Silicon based pulse rectifiers were initially used extensively, but since they suffer from slow rising and falling times and hence cannot deliver high pulse rates, they have grown into disuse. Also, feedback control of the current has been considered to maintain an applied current level. The previously developed tools for pulsed anodizing (with similar specifications to those needed for electroplating) are covered in the review by Raj *et al.*[9]

For direct current electrodeposition, the applied current density as a single parameter is controlled to a setpoint, while in pulsed electrodeposition, there is always a continuous variation of applied current density. Two categories of pulsed electrodeposition are generally used: ordinary pulsed electrodeposition, also referred to as unipolar pulsed electrodeposition, and pulsed reversed electrodeposition, also called bipolar electrodeposition.

In ordinary pulsed electroplating, the applied current oscillates repeatedly between two values, creating a series of pulses with equal amplitude and duration. In unipolar pulsed electroplating, all pulses have the same polarity, the current oscillating between a positive value (I_{Peak}) and zero. When a positive current is applied, it is denoted the on-time (T_{On}), and when no current is applied, it is referred to as the off-time (T_{Off}), both adding to the total pulse time (T_{Pulse}) with an average current of I_{Avg}. The duty cycle (γ) of the pulse is then the proportion of the on-time pulse to the total cycle time,[31]

$$\gamma = \frac{T_{\text{On}}}{T_{\text{On}} + T_{\text{Off}}}. \tag{1}$$

Typically for unipolar pulsed electroplating, T_{On} is in the range of ms, with a duty cycle >5%. Pulsed electroplating will deposit films with a rate equal to *DC* electroplating operating at the average current (I_{Avg}) level,

$$I_{\text{Avg}} = I_{\text{Peak}}\gamma. \tag{2}$$

Several waveforms of the unipolar pulsed electroplating have been investigated in the past,[9,15,29] some of which are shown in Fig. 1.

Typical pulses for unipolar pulsed electroplating are (i) superimposed pulses where the pulses are added on top of a constant value, (ii) duplex pulses where a series of pulses with a certain current density are followed by another series of pulses with a different current density, (iii) pulsed pulses where each pulse is composed of group of pulses, and (iv) pulsed on pulse where each pulse have a series of pulses built over it.

For bipolar pulsed electroplating, the current oscillates between values with different polarities. A positive current I_{Anode} for time T_{Anode} and a negative value I_{Cathode} for time T_{Cathode} adding to a total pulse time T_{Pulse} with an average current of $I_{\text{avg}}{}'$.[31,32] The duty cycle and the average current in the case of bipolar pulsed electroplating are given by[33]

$$\gamma' = \frac{T_{\text{Anode}}}{T_{\text{Anode}} + T_{\text{Cathode}}}, \tag{3}$$

$$I_{\text{Avg}}{}' = \frac{I_{\text{Anode}}T_{\text{Anode}} - I_{\text{Cathode}}T_{\text{Cathode}}}{T_{\text{Anode}} + T_{\text{Cathode}}}. \tag{4}$$

For bipolar pulsed electroplating, beside the ordinary bipolar pulse, other forms were introduced,[9,15,29] as shown in Fig. 2. The typical candidates are (i) pulse reverse with off period,[34] (ii) pulsed pulse reverse, and (iii) pulsed on pulse reverse and duplex reverse pulses.[28]

The average current density of any of these waves formed can be calculated by integrating the value of the current

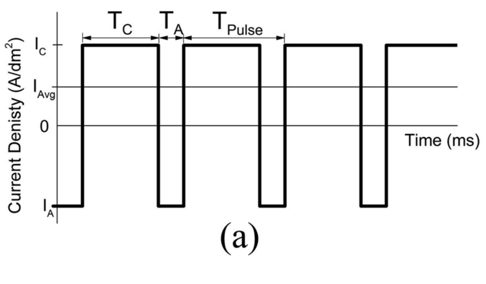

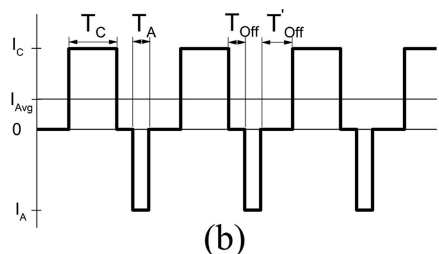

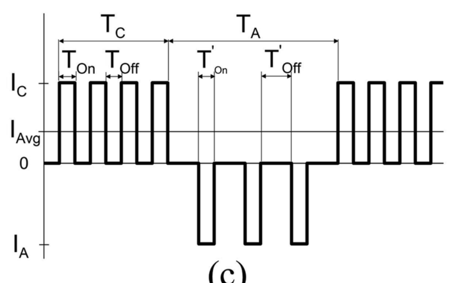

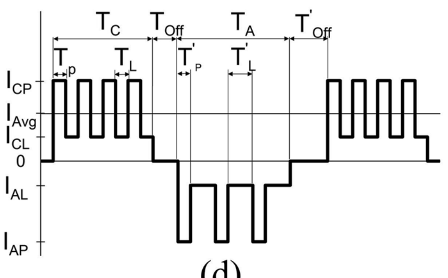

FIG. 2. Waveforms for bipolar pulsed electrodeposition: (a) reverse pulse, (b) with off-time, (c) pulsed reverse pulse, and (d) pulsed on pulse.

© Author(s) 2019

density provided through a single full pulse over the total time of the pulse,

$$I_{\text{Average}} = \frac{1}{T_{\text{Total pulse}}} \int_0^{T_{\text{Total pulse}}} I(t)dt. \quad (5)$$

Generating these complex waveforms in a way that is compatible with the electroplating process is challenging and hampers the benefit of the advantages that these waveforms produce in the electroplated film. Section IV shows that the developed systems are capable of robustly generating all of these waveforms when connected to an electroplating bath and also capable of providing relatively high current densities as well as relatively high switching rates (several kilohertz) as discussed in the Applications section.

III. ELECTRONICS DESIGN

A current source was developed to precisely control the amplitude and waveform of the current forced through the electroplating bath, as well as to record a feedback signal of the output voltage. The current circuit mainly consists of three modules: the first module is an isolated power supply to provide the circuit with the required power (12 V and 2 A), and the second module is to sense the feedback signal using microcontroller as well as controlling the voltage provided to the third module, which is a voltage controlled current circuit (*VCCC*).

The microcontroller sets the voltage by using a digital to analog converter (*DAC*) through a serial peripheral interface (*SPI*). A feedback signal from the output is connected to an analog to digital converter (*ADC*) and back to the microcontroller through the inter-integrated circuit (I^2C) protocol, as shown in Fig. 3. A 16 bit DAC (DAC8831, Texas Instruments®) is used and connected to a reference voltage of 2.5 V and hence can provide bipolar output ($\pm V_{REF}$) by connecting it to an external buffer. Since a bipolar *ADC* is used, the most significant bit (*MSB*) acts as a sign bit, while the rest of the acquired word defines the signal, as shown in the following equation:

$$Resolution = \frac{V_{\text{ref}}}{2^{n-1}}. \quad (6)$$

The feedback signal is also connected to an *ADC* (ADS1112, Texas Instruments) with the same number of bits. A real-time clock (*RTC*) integrated circuit (*IC*) (BQ32000, Texas Instruments) is connected to the microcontroller to keep track of the performed process in real time.

A BeagleBone Black Wireless® (*BBB*) is used as a microcontroller since adding a wireless module allows online access to the circuit, to remotely set the electroplating parameters, and, more importantly, to monitor the values of the output voltage, which are used for observing the connected load impedance.

The graphical user interface (*GUI*), as shown in Fig. 4, based on a Python script is preprogrammed with all the previously mentioned waveforms. The *GUI* is designed to allow the user to choose the required electroplating type as well as the waveform, which then activates a query for the parameters which are required to be set by the user. The user also defines the total time of the process and the area required to be electroplated. The script then calculates the current to be provided using the specified area and current densities. One advantage of the device is that it can autonomously run a series of different electroplating waveforms, which allows us to electroplate structures with several layers that have completely different microstructures, as discussed later (see Fig. 16). The measured output value, the currently running waveform, the total process time, and the remaining time are displayed on the GUI with real-time updates.

The third module (*VCCC*) is the most important part of the circuit as it defines the performance of the circuit. Several designs and approaches of the voltage controlled current source have been used before[35–41] in different applications. The main feature of a *VCCC* is the nominal value and stability of the output impedance while changing the output frequency or the connected load impedance. A current source derived from the modified Howland current source (*MHCS*) was developed, characterized, and subsequently used in our electroplating experiments.

A. High power OPAMP circuit (modified Howland current pump)

The modified Howland current source (*MHCS*) is commonly used in applications that require high stability for a controlled current over a wide range of frequencies (Fig. 5). The *MHCS* can source or sink a highly precise amount of bipolar current, providing a high output impedance within a broad frequency band. The MHCS has been used in many applications in different fields, e.g., in electrical impedance tomography (*EIT*) to detect breast cancer,[42] in

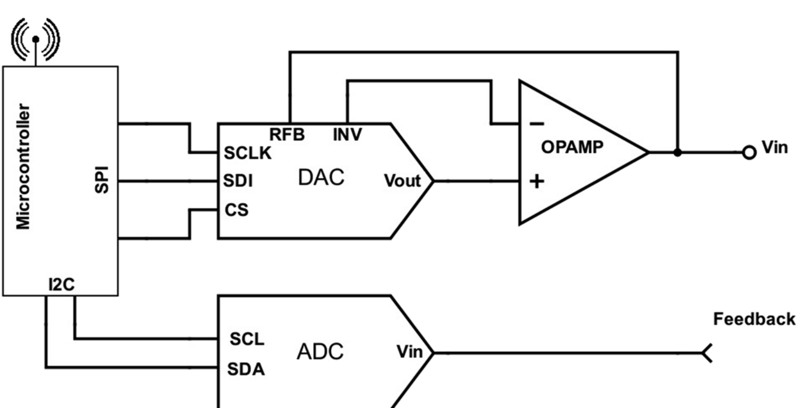

FIG. 3. A schematic figure of the circuit (i) controlling the input voltage to the *VCCC* and (ii) measuring the feedback signal.

© Author(s) 2019

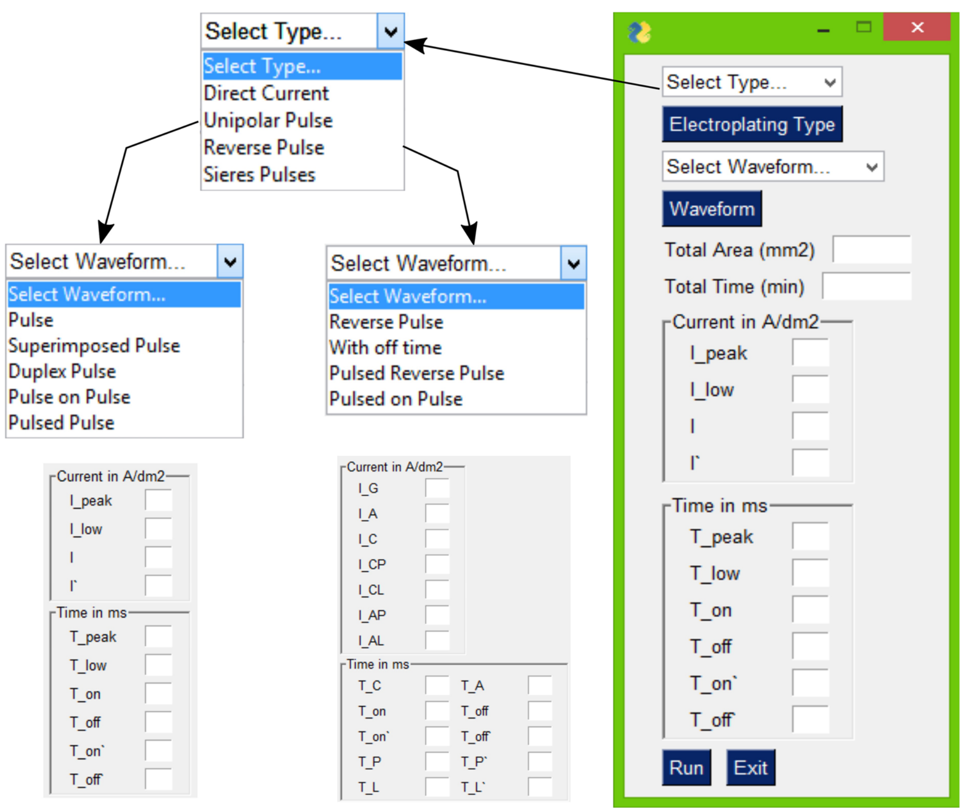

FIG. 4. Graphical user interface (*GUI*). The user can choose the type and waveform of the electroplating process and insert the electroplating parameters.

functional neural stimulation (*FNS*),[43–45] in tissue characterization by electrical impedance spectroscopy (EIS),[46] bioimpedance measurements,[47] as well as in capacitive sensors with single electrode,[48] and works with grounded or floating loads.[49]

Bradford Howland first introduced the Howland current source (*HCS*) in 1962[50] for controlling current via voltage; however, it suffered from some weakness, especially regarding the voltage compliance, since the output voltage does not swing close to the rail voltage.[51] Another weakness is that it is inefficient when the load acquires a high voltage, in which case it wastes power, so that the modified (*MHCS*) version was introduced, where the loading effects or the common mode voltages were eliminated by connecting the output and noninverting ports of the amplifier (*OPAMP*) using a resistor.

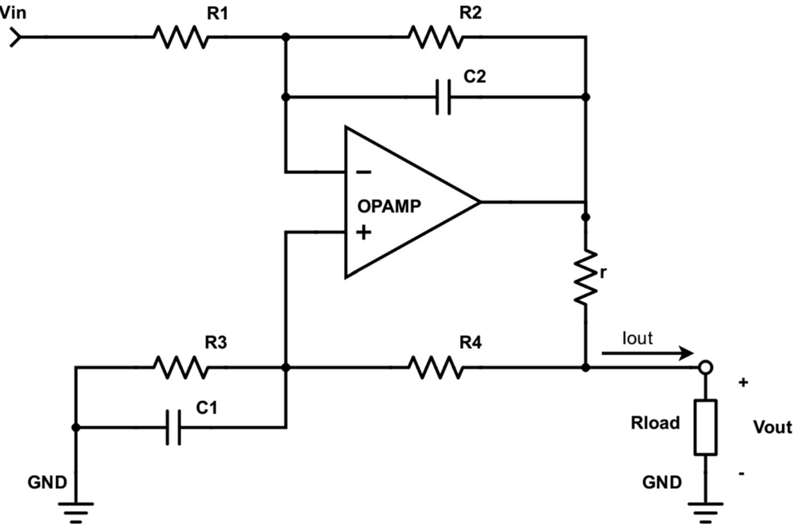

FIG. 5. A schematic drawing of the modified Howland current source (MHCS).

© Author(s) 2019

To control the current accurately over a wide range of frequencies, two approaches are commonly used: either a current mirror architecture is employed to sense the output current of the operational amplifier (*OPAMP*), but with the need for a positive feedback, or a modified Howland circuit is used which provides a positive feedback. A comparison between the modified Howland circuit and the mirror current source can be found in Ref. 37.

The modified Howland current source has been chosen for its simplicity, stability, voltage compliance, and reliable performance under different conditions; several studies were done for testing its performance under different conditions, such as investigating the performance stability under different frequencies up to 10 MHz,[49] noise analysis,[52] and the influence of temperature on the output.[53] Usually, these studies were performed because the actual performance deviated from prediction due to ideality assumptions. Several comprehensive studies of the Howland current pump have been performed, including a discussion of the practical problems involved.[51,54]

The modified Howland current circuit consists mainly of two passive components (set of resistances and capacitors) and one active component [the operational amplifier (*OPAMP*)]. In order to achieve an *MHCS* with high performance that has a stable output current, a high output impedance, and a broad bandwidth, these components must be chosen carefully. The main factors which affect the performance of the circuit are the tolerance in the resistance values and the degree of nonideality of the OPAMPs.

Using straightforward circuit analysis with assuming an ideal *OPAMP*, the output current I_{out} is expressed as a function of the input voltage (V_{in}) in Eq. (7). The following equation reveals a simple linear relation:

$$I_{\text{out}} = -V_{in}\frac{R_2}{R_1 r} + V_{out}\frac{R_1(R_4 + r) - R_2 R_3}{R_1 r(R_3 + R_4)}. \tag{7}$$

One of the main requirements of a high precision current source is to have a high output impedance compared to the load through which current should pumped so that the value of the output current is not affected by the load impedance. The output impedance can be derived by V_{out}/I_{out} while connecting V_{in} to the ground. The output impedance should therefore have a value of a few megaohms for single digit voltages and currents,

$$Z_{out} = \frac{R_1 r(R_3 + R_4)}{R_1(R_4 + r) - R_2 R_3}. \tag{8}$$

Because of the nonideal performance of the OPAMP of having a finite Common-Mode-Rejection-Ratio (CMRR) which is the ratio between the differential gain (A_d) and the common mode gain (A_{CM}), it contributes to the output signal with a part known as common mode noise. The part of the CMRR becomes of importance when the differential input (V_d) is comparable to the common-mode input signal (V_{CM}),

$$V_{out} = V_d A_d + V_{CM} A_{CM},\, CMRR = \frac{A_d}{A_{CM}}. \tag{9}$$

In the application of electroplating, the effect of the *CMRR* becomes clear when a small output signal of few milliamperes is required for electroplating microstructures. It is preferable for the *MHCS* to choose the resistance in a way to increase the close loop *CMRR* to being able to suppress the common-mode input signal as the mismatch of the resistors will result in low *CMRR*, no matter how good the OPAMP is. The close loop *CMRR* as a function in the resistors can be derived by assuming a nonideal OPAMP with finite gain (A); then, the output is calculated in the presence of inputs on the positive and negative terminals of the amplifier,[54]

$$CMRR = 1 + 2A\left(\frac{R_1}{R_1 + R_2} + \frac{R_4}{r}\right). \tag{10}$$

The effect of the resistance tolerance on the output impedance (Z_{out}) and the common mode rejection ratio *CMRR* is studied by in Refs. 54 and 55. Z_{out} and the *CMRR* both are inversely proportional to the tolerance, and as the used resistances have wide ranges of tolerance, the performance of the circuit is strongly reduced by decreasing both Z_{out} and *CMRR*. A small value of r improves the *CMRR*, but at the same time, it reduces Z_{out} in Eq. (8). The circuit should rather be designed to be symmetrical to increase the stability. By choosing $R_1 = R_3$ and $R_2 = R_4 + r$ so that R_1/R_2 matches $R_3/(R_4 + r)$, we can achieve the goal that the total output current in Eq. (7) will not be dependent on the output voltage and can be expressed as

$$I_{out} = -V_{in}\frac{R_2}{R_1 r}. \tag{11}$$

The gain is set by r and scaled by R_1/R_2. The value of r is usually low in the range of a few to hundred ohms, and the remainder of the resistances is in the range of kilo-ohms to megaohms. Also, $R_2 \gg r$ so that the direction of the current can be assumed to flow through the load according to the current divider rule.

Trimming the resistances can result in increased performance of the *MHCS* as it leads to a higher *CMRR* and increases the stability of the output current by overcoming the dependency on voltage. To accurately set the resistance values, trimmer resistors can be used, as well as highly accurate resistors which are expensive; other ways for trimming the resistance are mentioned here.[51] A potentiometer can be used in series with R_3 to balance the gain so that the current can be controlled with a resolution in the microampere range, with voltages up to a few volts, in an efficient manner.

In general, any OPAMP can be used in the *MHCS*. For the case that a wide range of output voltages are needed, OPAMPs with a supply voltage range of ± 15 V should be used. Low voltage CMOS amplifiers can be used in the case of low output voltage. Current feedback amplifiers work at low impedance and usually have insufficient *CMRR*, even below 60 dB. They require excellent trimming to balance the weak *CMRR* but can act as very fast current pumps.

A feedback capacitor C_2 in parallel with the feedback resistance R_2 must be added to provide a single dominant pole in the negative feedback loop, so as to prevent sustained oscillations by narrowing the bandwidth and hence remove the higher frequency noise. Adding the capacitor creates a low pass filter with a cutoff frequency calculated by Eq. (12). Choosing a capacitor with a value of a few nanofarads is always preferred, in order to decrease the bandwidth and thereby enhance the output stability, but also it slows down the output. When a wider bandwidth is necessary, capacitors with values down to few picofarads can be used instead,

© Author(s) 2019

TABLE I. The component values used in the designed modified Howland current source (MHCS).

Component	Value
Opamp[a]	OPA561
$R_1 = R_3$	6800% ± 1% Ω
R_2	10% ± 1% kΩ + 10% ± 5%Ω
R_4	10% ± 1% kΩ
r[b]	10% ± 5% Ω
C_1	3 pF
C_2	15 pF

[a]High power *OPAMP*.
[b]Thick film power resistor (PWR163 Series Power Resistor) with 25 W rating power.

$$f_{\text{cutoff}} = \frac{1}{2\pi C_2 R_2}. \tag{12}$$

A capacitor between the OPAMP's positive input and ground is added to ensure that the positive feedback is always less than the negative feedback so as to provide stability under open output conditions. A generalized impedance converter can be added to cancel the parasitic capacitance, but it affects the stability at high frequencies.[56]

The dynamic behavior of the *MHCS* can be estimated based on the virtual capacitance of the circuit, as shown in Eq. (13),

$$C_{out} = \frac{I_{out}}{dV_{out}/dt} = \frac{R_3(R_1 + R_2)^2}{2\pi r R_1^2 (R_3 + R_4) GBWP}. \tag{13}$$

The virtual capacitance of the *MHCS* can be derived by applying a voltage changing with time at the output node of the circuit and a small signal at the amplifier input;[51] then, the output current is calculated which in this case serves as capacitive current. Increasing r or using an *OPAMP* with high Gain Band Width Product (*GBWP*) decreases the virtual capacitance of the circuit, which increases output speed.

1. Characterization of the designed MHCS

Since resistors with excellent tolerances of ±1% were chosen, no trimming was needed (Table I). A high power resistor with 25 W rating power is used for r as the output current will be going through it. The maximum output current of the circuit is below 370 mA, so the maximum power dissipated in the resistor is way below its rating power. Therefore, the resistor's temperature does not increase much insuring the constant value of r. Based on the value shown for the negative feedback capacitor C_2, the *MHCS* in isolation can work up to a frequency of more than 1 MHz based on Eq. (12). A high power amplifier (OPA561) with a maximum output current of 1.2 A is used. This amplifier has a thermal shutdown option which is important for the electroplating applications where electroplating processes are running continuously; also it possesses a status pin (E/S) which gives a signal in the case of thermal shutdown. A sufficiently powerful cooling system should be provided to the circuit to avoid shutdown conditions of the *OPAMP*, also to ensure stability in performance, especially when running a long electroplating process with relatively high current densities.

As shown in Fig. 6, a fan was used. Also, we implemented a cooling pad with holes in the printed circuit board (*PCB*) under the amplifier. For determining the required heatsink area, first the power dissipation (*PD*) through the *OPAMP* is calculated as shown in the following equation:

$$PD = P_{Supply} - P_{Load} = V_S I - I^2 R_{Load}. \tag{14}$$

The power dissipated in the amplifier is the difference between the power supplied (P_{Supply}) and the power given to the load (P_{Load}). Since the power delivered to the load is proportional to the square of the output voltage, the maximum PD occurs at half of the supplied voltage,[57] and in this case, $I = V_S/2R_L$. Hence, the maximum power dissipated in the amplifier equal to

$$PD_{max} = \frac{V_S^2}{2R_L}. \tag{15}$$

Based on Eq. (15), the maximum dissipated power in the amplifier of our circuit is around 1.25 W. The junction temperature (T_J) can be calculated using the dissipated power, junction to ambient thermal resistance (θ_{JA}), and the ambient temperature (T_A), as shown in the following equation:

$$T_J = PD\theta_{JA} + T_A. \tag{16}$$

FIG. 6. The implemented current supply circuit featuring and isolated power supply, bipolar DAC for generating the control voltage signal, and the voltage controlled current source (VCCC).

© Author(s) 2019

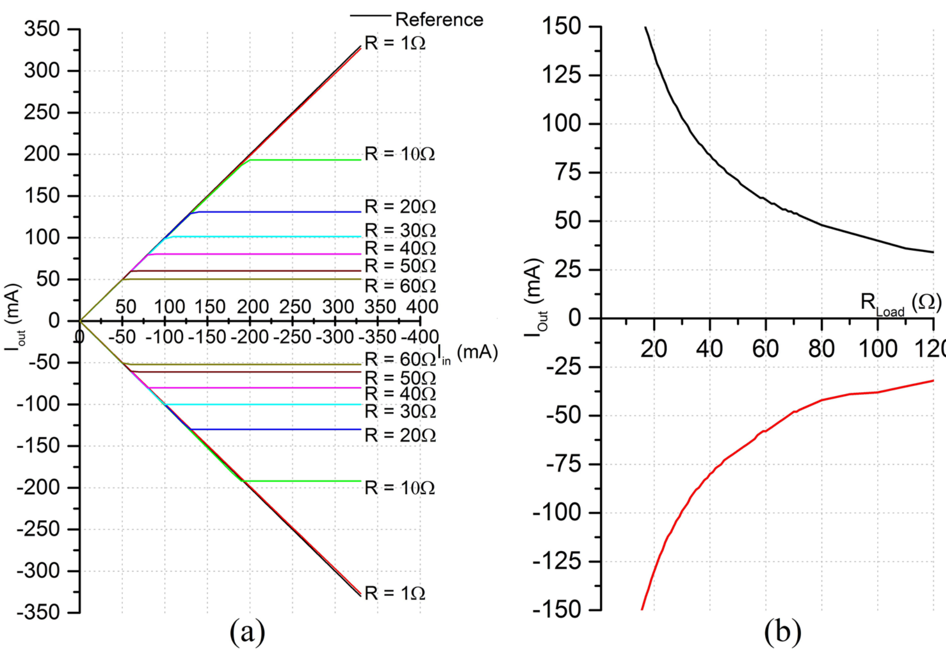

FIG. 7. The experimental data from measuring the effect of the connected load on the output current: (a) the programmed output current and its measured value at different load resistances and (b) the maximum output current at different load resistances.

θ_{JA} (°C/W) is a function in the heatsink area and is provided in the datasheet of each device. Hence, the junction temperature of our amplifier in the case of maximum power dissipation at room temperature of 25 °C is around 85 °C which is below the maximum junction temperature of OPA561 which is 150 °C.

The output currents and voltages of the circuit were tested under different load resistances. Additionally, the time response of the circuit was measured when switching between different current levels.

Figure 7(a) shows the relationship between the programmed current I_{in} and the measured output current I_{out} when varying the load resistance. The reference line shows the ideal performance; a deviation from this line is the error value. The error increases proportionally with the output current value I_{out}, with the measured error values in the range of 0%–2%, until the maximum driving voltage is reached and the current does not increase. The maximum output current decreases with increasing load resistance. Figure 7(b) shows the maximum output current I_{out} at each load resistance value. Usually, the electroplating setup has a resistance of only a few ohms, and hence, the full range of the current can be used for the electroplating process.

For practically all current sources, there is a saturation value of the output voltage $V_{saturation}$ below which the output current is constant. Above $V_{saturation}$, the output current I_{out} starts dropping, as shown in Fig. 8. This represents the typical behavior of many current sources, where at low load, the current is constant, and as the load increases, the current starts following the dropping curve. For the designed circuit, the saturation voltage was measured to be ±4.3 V, which is an excellent performance for an *OPAMP* supplied with voltages of ±5 V.

For pulsed electroplating, the output current I_{out} always oscillates between varying values, and hence, the settling time, overshoot, and final error of the output are of interest. The change in these three factors with respect to the difference between the output levels, as well as while changing the load resistance R_{out}, is illustrated in Fig. 9. At low output current, the circuit requires around 30 μs to settle to its final value. The settling time decreases as the value of the output current increases, as shown by the three families of

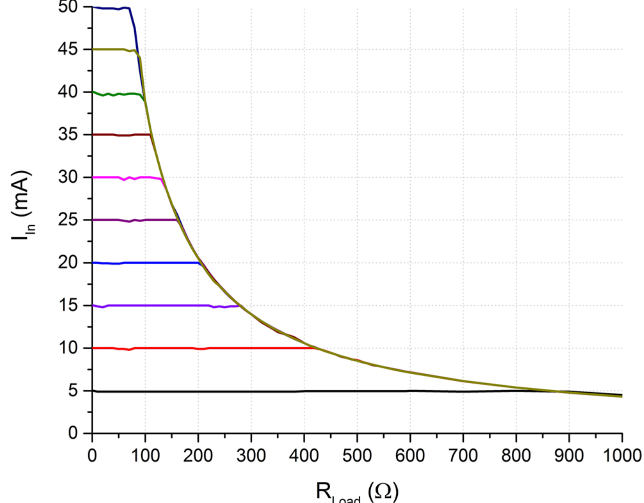

FIG. 8. Saturation curves experimentally acquired, showing the current drop for different values of the load resistance.

© Author(s) 2019

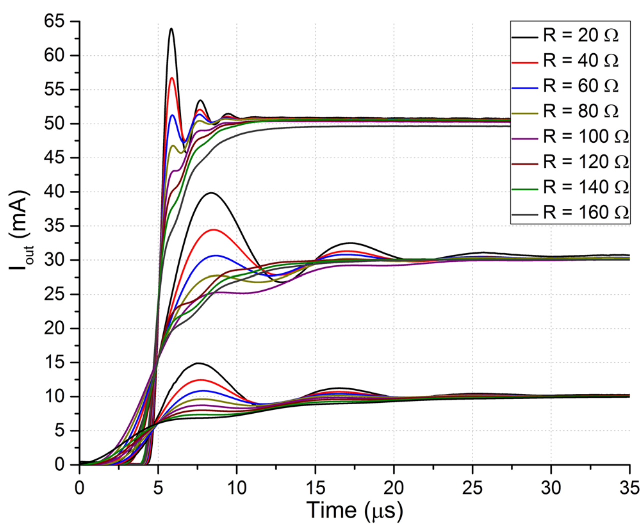

FIG. 9. The measured settling time of the output current at different load resistances and current levels.

curves. Increasing the load resistance increases the settling time as well. On the other hand, a higher load resistance dampens the overshoot value, which otherwise increases with increasing output current.

IV. APPLICATIONS

A. Generating electroplating waveforms

The electroplating capability of the circuit was tested by applying the waveforms discussed in Sec. II and in Figs. 1 and 2. The cathode of the current source was connected to a copper electrode, while the anode was connected to a uniformly metallized silicon wafer of rectangular shape, with dimensions of 4 cm × 1.5 cm. The wafer was prepared with a layer of 20 nm chromium and 60 nm gold, which were deposited by physical vapor deposition (*PVD*, Univex 450), at deposition rates of 5 Å/s and 8 Å/s, respectively. Both electrodes were immersed in a self-made sulfuric acid based electrolyte bath (Cuprostar® LP-1, Enthone-OMI GmbH), which was constantly stirred as well as filtered by an electric pump setup. Relatively high current densities of 6 A dm^{-2} were applied, as shown in Figs. 10 and 11.

The ripples and oscillations on the measured signals are barely visible because of the time scaling. The pulse widths were chosen in a way that fits with the electroplating application. During the electroplating process, the pulse width should be enough to charge a layer between the substrate and the electrolyte; this layer is called the electric double layer (*EDL*); otherwise, electrodeposition will not happen. Hence, enough time should be provided for the metal to deposit; usually, this process is in the range of tens of milliseconds, and also the negative pulse should be enough for the interface to discharge. The purpose of these examples was to demonstrate

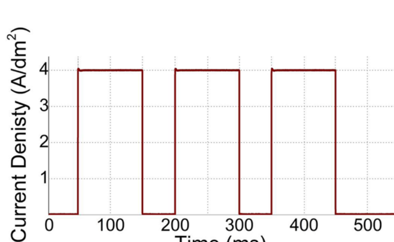

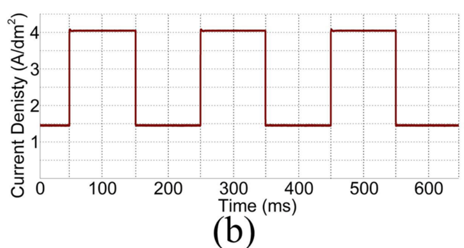

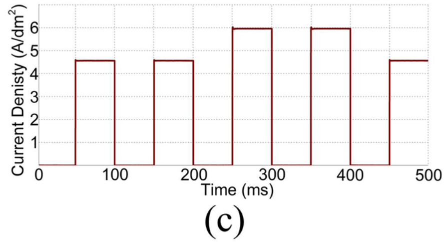

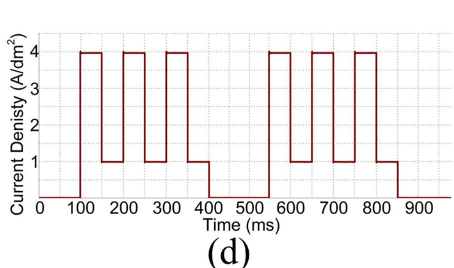

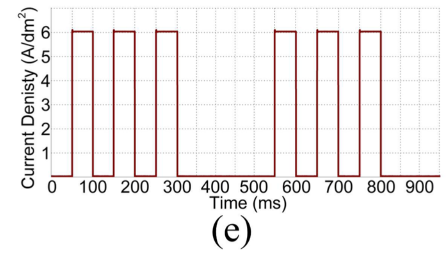

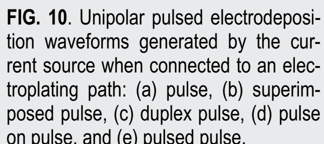
FIG. 10. Unipolar pulsed electrodeposition waveforms generated by the current source when connected to an electroplating path: (a) pulse, (b) superimposed pulse, (c) duplex pulse, (d) pulse on pulse, and (e) pulsed pulse.

© Author(s) 2019

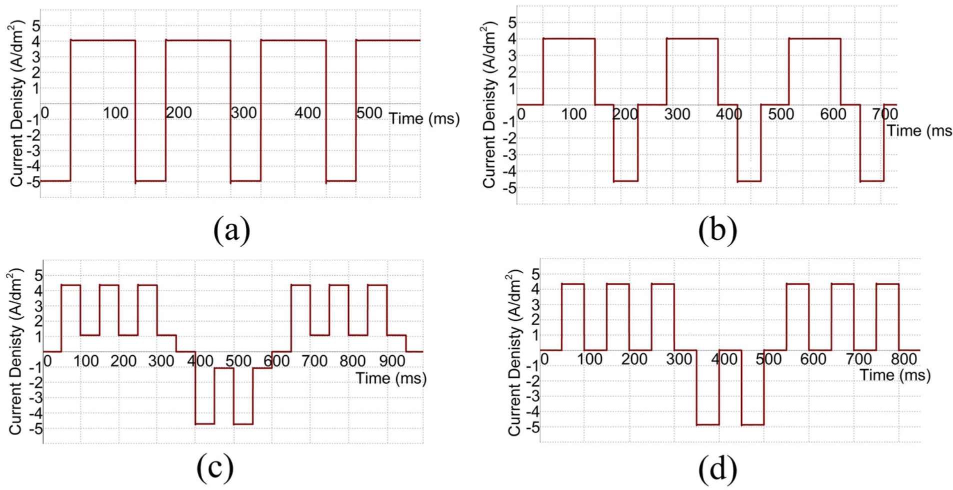

FIG. 11. Bipolar pulsed electrodeposition waveforms generated by the current source when connected to an electroplating path: (a) reverse pulse, (b) with off-time, (c) pulsed reverse pulse, and (d) pulsed on pulse.

the capability of the device under extreme conditions. The circuit worked in a stable and robust way in applying all indicated electroplating waveforms, running for more than 2 h. We also successfully tested the ability to apply the same waveforms with different time intervals and current densities.

B. Printed flexible electronics

Electroplating plays an important role in the area of printed flexible polymers,[58] in which the integration of metallic conductors with conductive polymers onto and into polymer substrates is the key challenge. The printing of a conductive material onto foils leads to low cost, light weight, flexible, and yet complex electronic components. The market of printed electronics had a turnover of up to 24$ billion in 2014 and is predicted to have a bright future with a growth rate of 20% per year for the upcoming years.[59]

Printed metal traces can, for example, be constructed by the inkjet printing of metal nanoparticles,[60] leading to conductive tracks of widths in the range of tens of micrometers. After printing, the conductive ink needs to be sintered which, typically, requires high temperatures (>150 °C) for durations of more than 30 min, placing constraints on possible substrate materials. Alternative lower temperature sintering methods have also been studied[61] but have not yet become mainstream. Since the printed inks contain large amounts of solvent, inkjet printed and sintered tracks have thicknesses in the range of hundreds of nanometers. Such tracks are not useful for applications which required high metallic conductivities in the DC to radiofrequency range because high resistances generate Joule heat losses and introduce thermal noise during electrical signal transfer for applications requiring a minimum skin depth of the conductor shown in the following equation:

$$\delta = \sqrt{\frac{\rho}{\pi f \mu}}. \quad (17)$$

Here, δ is the skin depth, f is the electrical signal's frequency, ρ and μ are the resistivity and permeability of the conductor material.

Increasing the thickness of the conductive layer can be done either by printing multilayers[62] or by electroplating which has proven to be more efficient. Moreover, it allows increasing the thickness to several micrometers.[4,63,64]

The adhesion of metallic films on the substrate is particularly challenging. Inkjet printing applies inks to the top surface of a substrate, and with insufficient adhesion, immersion in the electroplating bath under application of a DC current can lead to peeling of the printed traces from the substrate, as shown in Fig. 13. The charged layer created around the electroplated tracks leads to high current concentrations along the edges and corners of the tracks,[15] and the resulting plating stress leads to peeling off of the structures. Controlling this charged layer via pulsed electrodeposition is a remedy and one of the primary reasons for the application of differentiated electroplating voltage waveforms.

1. Experiment and results

We tested the different electroplating waveforms to determine their effect on adhesion on flexible Kapton substrates, as well as on the metallic microstructure that resulted from plating. Silver rectangles of dimensions 10 mm × 13 mm were printed on a 125 μm thick polyimide film, an example of which is shown in Fig. 12.

The ink used was 30–35 wt. % suspension of silver nanoparticles with a diameter ≤50 nm dispersed in triethylene glycol monomethyl ether, purchased from Sigma-Aldrich®. The ink is rated with a viscosity of 10–18 mPa s and a surface tension of 35–40 mN m^{-1}, determined at room temperature.

The printing was performed using a Fujifilm Dimatix DMC-2800 printer, loaded with a 10 pL print head cartridge (DMC-11610, Fujifilm Dimatix). One nozzle was used for printing and maintaining the head and substrate at temperature of 28 °C. The dot spacing was set to 35 μm, and the printing frequency was set to 5 kHz, which resulted in uniformly printed lines.

Before printing, the Kapton film was cleaned appropriately with acetone, isopropyl alcohol (*SPI*), and deionized water (*DI water*). After printing, the sample was transferred to a hotplate and dried at 80 °C for 15 min followed by sintering in an oven for 1 h at

© Author(s) 2019

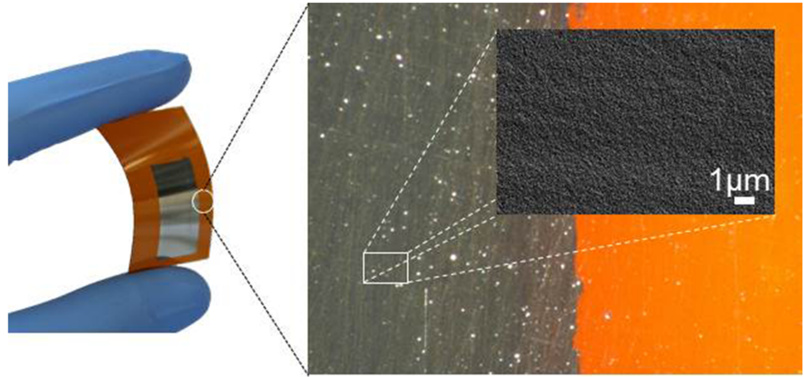

FIG. 12. Inkjet printed silver patch on a polyimide film shown for three levels of detail. The inner zoom is a scanning electron micrograph (SEM) with a magnification of ×20 K.

150 °C. Subsequently, electroplating was carried out in a self-built sulfuric acid-based-electrolyte bath (Cuprostar LP-1, Enthone-OMI GmbH), which was constantly stirred as well as filtered by an electric pump. Electroplating was done without heating the bath, or additives, since the interest here was to control the electroplating output by controlling the waveform only. After electroplating, the samples were cleaned by spraying them using DI water and *SPI*, followed by placing the sample in a vacuum for 20 min for drying.

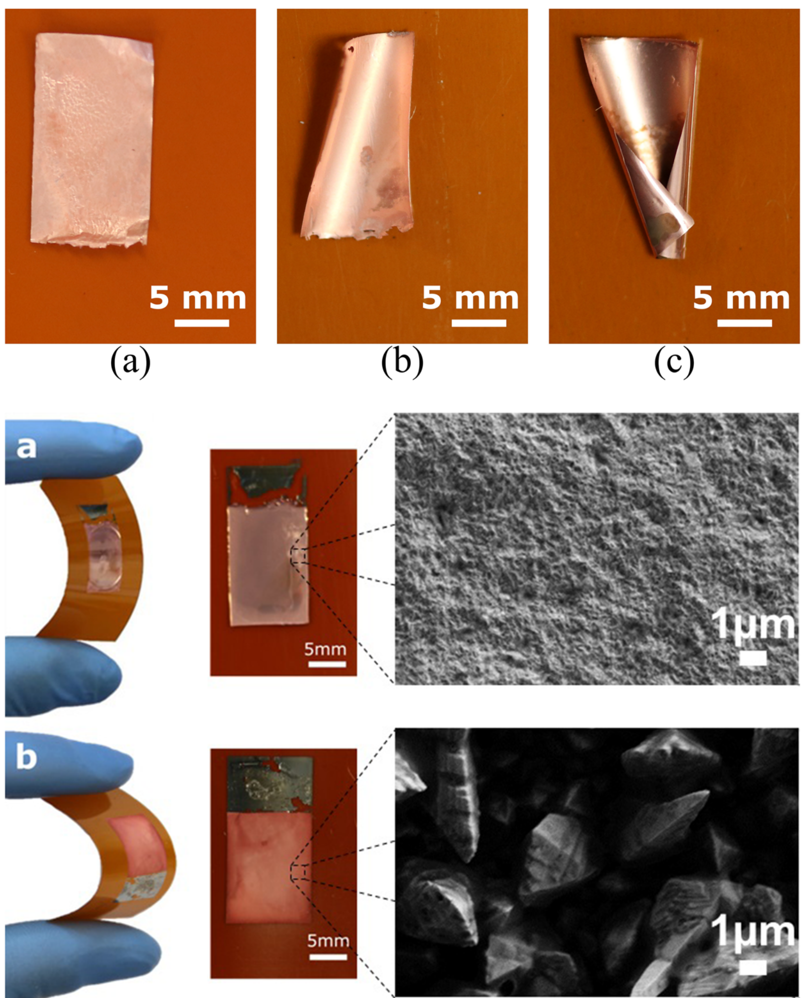

FIG. 13. DC electroplating of inkjet printed silver tracks using different current densities: (a) low, (b) medium, and (c) high current densities. The stress-induced curling of the films is seen in (b) and (c).

FIG. 14. (a) Unipolar and (b) bipolar electroplating of the printed silver tracks with *SEM* images of ×20 K magnification.

© Author(s) 2019

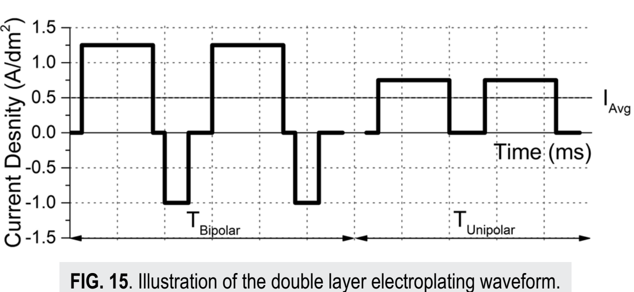

FIG. 15. Illustration of the double layer electroplating waveform.

The samples were electroplated using DC waveforms with relatively low, medium, and high current densities of 0.5 A dm^{-2} for 90 min, 1.5 A dm^{-2} for 30 min, and 3 A dm^{-2} for 15 min, resulting in a copper films of thicknesses of ≈10 μm. As shown in Fig. 13, all the samples subjected to DC waveform electroplating peeled off from the substrate. It was also observed that as the current density increased, the structures start to roll up due to internal stress.

Then, samples were electroplated with unipolar and bipolar with off-time waveforms. The parameters of the unipolar pulse were I_{Peak} = 0.6 A dm^{-2}, T_{ON} = 250 ms, and T_{OFF} = 50 ms. The parameters of the bipolar pulse were I_C = 0.8 A dm^{-2}, I_A = 1.5 A dm^{-2}, T_C = 300 ms, T_A = 50 ms, T_{Off} = 10 ms, and T'_{Off} = 20 ms. Both types of waveforms have an average current density of 0.5 A dm^{-2}, resulting in the same deposition rate. The processes were run for 90 min, resulting in a copper film of thickness ≈10 μm.

The microstructure change resulting from two waveforms was investigated with respect to their surface topography and roughness, as well as the grain size, using three characterization techniques: (1) scanning electron microscopy (Carl Zeiss AG—SUPRA 60VP SEM), with images shown in Fig. 14 at a magnification of 20 K; (2) white light interferometry (Bruker ContourGT-K 3D Optical Microscope), to measure the surface roughness focusing over an area of 75 μm × 95 μm, the size chosen to avoid the bending of copper sheets from affecting the calculation of roughness. The unipolar and bipolar electroplated samples showed roughness values of 51 nm and 1840 nm, respectively; and (3) X-ray diffraction was conducted on a Bruker D8 Advance diffractometer in $\theta - \theta$ geometry using Cu-K$\alpha_{1,2}$ radiation measured in the range between 40° and 99°. Crystallite sizes (L_a) were determined according to the Scherrer formula, based on a method described by Warren.[65] Sizes for the unipolar and bipolar electroplated samples were 30 nm and 307 nm, respectively.

The developed setup allows us to run a series of electroplating processes with different waveforms, achieving electroplating films with several layers having individually determined microstructures. As indicated in Fig. 15, a series of bipolar and unipolar electroplating was performed for a printed silver track to combine the advantage of the bipolar waveform, preserving adhesion to the substrate, and a unipolar waveform toward a smooth surface. The bipolar waveform (I_C = 1.25 A dm^{-2}, I_A = 1 A dm^{-2}, T_C = 250 m s, T_A = 100 ms, T_{Off} = 25 ms, and T'_{Off} = 50 ms) ran for $T_{Bipolar}$ = 15 min and the unipolar waveform ($_{Peak}$ = 0.8 A dm^{-2}, T_{ON} = 250 ms, T_{OFF} = 150 ms)

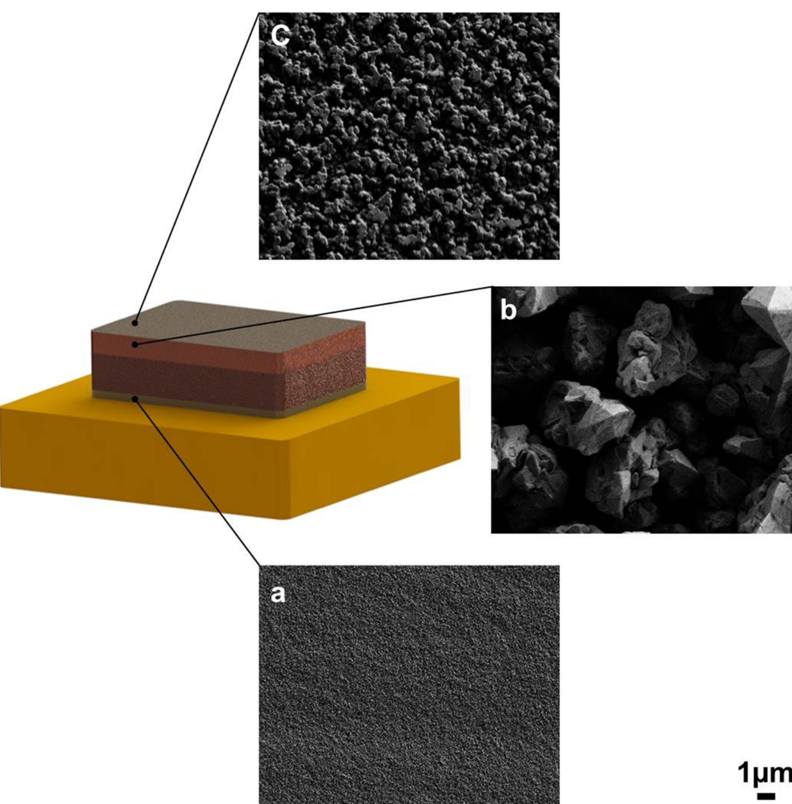

FIG. 16. Double layer electroplating of a printed silver track. The dimension bar to the lower right refers to the SEM micrographs: (a) printed silver layer, (b) bipolar electroplated layer for good adhesion but resulting in a rough surface, and (c) unipolar electroplated layer with relatively smooth surface.

© Author(s) 2019

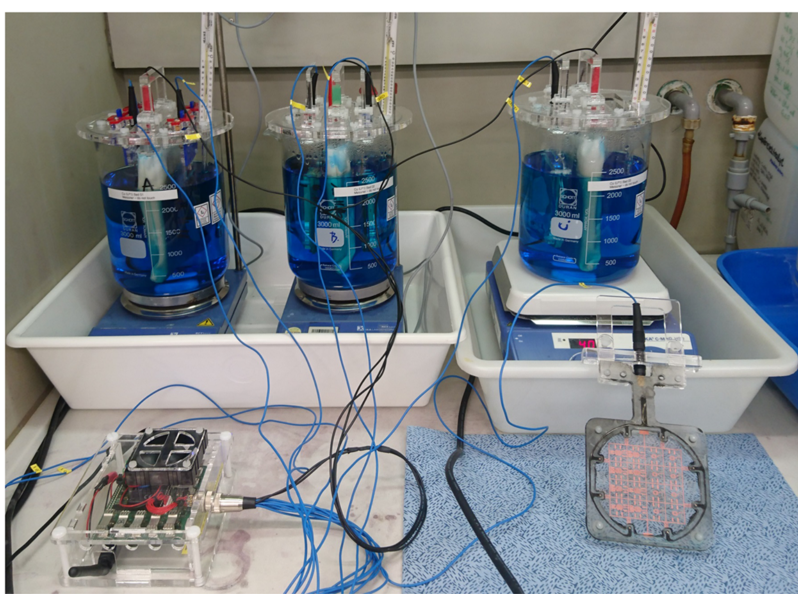

FIG. 17. Setup for electroplating eight 4 in. wafers in parallel. The power supply is shown in the foreground left, a wafer holder is shown to its right.

for $T_{Unipolar}$ = 75 min. Both pulses had an average current density of 0.5 A dm^{-2}, resulting in a copper film with a total thickness of ≈10 μm.

SEM revealed the structure of both layers, as shown in Fig. 16, where the bottom layer resulting from the bipolar pulse had a relatively rough surface but resulted in good adhesion of the track to the substrate, while the upper layer resulting from the unipolar pulse featured a smoother surface. The roughness of the upper surface was measured by white light interferometry to be 328 nm.

C. Parallel electroplating

A self-constructed setup was prepared for parallel electroplating of eight 4 in. wafers, in a sulfuric-acid-based electrolyte. A current source with eight separate current channels was used, each being separately and real-time controllable (Fig. 17).

Holders for the anodes, cathodes (wafers), thermometers, and electric connections were made out of *PMMA* sheets cut into the required shapes using a laser cutter (VLS2.30, Universal Laser Systems Inc.). The holders of the copper anode and the plated samples were designed to place them securely in the proper relative spatial position.

The copper anodes (phosphorus content of 0.04%–0.06%, Galva-Metall GmbH, Rödermark) were cut in shapes of 150 mm × 120 mm × 10 mm. The immersed area of the anode was 120 mm × 120 mm which was adjusted to the 4 in. substrates. Since the copper anode slowly dissolves in the absence of the applied plating current, it was removed from the bath and stored in a 10% H_2SO_4 solution when no plating was performed. The copper anode was wrapped in a polypropylene anode filter bag (PP8935, Winkler Filtration Technology GmbH) to retain copper particles larger than 20 μm and prevent them from plating.

The micro-electroplating bath used here was based on the Cuprostar LP-1 electrolyte system (Enthone-OMI GmbH), originally targeting PCB fabrication. The electrolyte allowed plating at room temperature at current densities of up to 3 A dm^{-2}.

The electrolyte was poured in four 3l glass beakers, each equipped with one copper anode and two wafers connected to the cathodes. The bath temperature was kept at 40 °C, which allowed plating at current densities of up to 40 mA cm^{-2}. Electroplating in heated electrolytes was reported by.[1] The electrolytes were constantly stirred by magnetic mixers. The plated copper achieved an electrical conductivity of 57.4 × 10^6 S m^{-1}.

V. CONCLUSION

Pulsed electrodeposition has been explored extensively in recent years for *PCB* and microfabrication and is also the basis of industrial scale micromanufacturing processes. Pulsed and pulse reversed electroplating has proved to have many advantages over conventional direct current electroplating; however, there is still room to further explore complex pulsed electroplating waveforms.

We presented a flexible and programmable current source for pulsed electroplating, with demonstrated stable and robust output power, even when operating under a variety of frequencies and current densities, which allows extensive freedom of plating parameter specification.

We demonstrated the use of our setup to solve a delamination issue when electroplating printed conductive tracks on unstructured flexible substrates, as well as to control the microscale structure of the deposited layer. The developed system was then used to successfully carry out a parallel electroplating recipe for eight 4 in. wafers in parallel, which saved time, materials, and effort.

We believe that the setup is straightforward and cost-effective to implement so that it can be copied and used in any laboratory which possesses moderate electronic skills.

© Author(s) 2019

SUPPLEMENTARY MATERIAL

See supplementary material for the power supply schematic design and board layout. The shell configuration file of the BeagleBone platform and the main Python code are attached. A read me file is included to navigate the user through the materials.

ACKNOWLEDGMENTS

The authors thank their KIT colleagues Emil Mamleyev for the help he provided with the *SEM* images, Richard Thelen for providing the white light interferometer measurements, and Peter Weidler for his support in acquiring the *XRD* measurements. The authors would also like to express their gratitude to the Microworks GmbH staff for providing the electrolyte used, the experience provided by the electroplating teams at IMT in Karlsruhe, and IMTEK in Freiburg. O.N. sincerely acknowledges financial support from the DAAD-GERLS program. S.W. thanks the support of the DFG through the project MetaCoils (Grant No. 227997126). The authors would like to express their gratitude to the DFG that supported the research through the Excellence Cluster 3D Matter Made to Order (3DMM2O).

REFERENCES

[1] M. Schlesinger and M. Paunovic, *Modern Electroplating* (John Wiley and Sons, 2011), Vol. 55.
[2] U. Erb, K. T. Aust, and G. Palumbo, "Electrodeposited nanocrystalline metals, alloys, and composites," in *Nanostructured Materials*, 2nd ed. (Elsevier, 2007), pp. 235–292.
[3] S. Franssila, *Introduction to Microfabrication* (John Wiley and Sons, 2010).
[4] M. V. Meissner, N. Spengler, D. Mager, N. Wang, S. Z. Kiss, J. Höfflin, P. T. While, and J. G. Korvink, "Ink-jet printing technology enables self-aligned mould patterning for electroplating in a single step," J. Micromech. Microeng. **25**, 065015 (2015).
[5] P. C. Andricacos, "Copper on-chip interconnections," Electrochem. Soc. Interface **8**, 6 (1999).
[6] I. Gurrappa and L. Binder, "Electrodeposition of nanostructured coatings and their characterization—A review," Sci. Technol. Adv. Mater. **9**, 043001 (2008).
[7] S. Tjong and H. Chen, "Nanocrystalline materials and coatings," Mater. Sci. Eng.: R: Rep. **45**, 1–88 (2004).
[8] D. Landolt and A. Marlot, "Microstructure and composition of pulse-plated metals and alloys," Surf. Coat. Technol. **169**, 8–13 (2003).
[9] V. Raj, M. Rajaram, G. Balasubramanian, S. Vincent, and D. Kanagaraj, "Pulse anodizing—An overview," Trans. IMF **81**, 114–121 (2003).
[10] N. Ibl, J. C. Puippe, and H. Angerer, "Electrocrystallization in pulse electrolysis," Surf. Technol. **6**, 287–300 (1978).
[11] T. Nakanishi, M. Ozaki, H.-S. Nam, T. Yokoshima, and T. Osaka, "Pulsed electrodeposition of nanocrystalline CoNiFe soft magnetic thin films," J. Electrochem. Soc. **148**, C627–C631 (2001).
[12] E. Tóth-Kádár, I. Bakonyi, L. Pogány, and Á. Cziráki, "Microstructure and electrical transport properties of pulse-plated nanocrystalline nickel electrodeposits," Surf. Coat. Technol. **88**, 57–65 (1997).
[13] J. Kelly, M. Cantoni, and D. Landolt, "Three-dimensional structuring of electrodeposited Cu-Co multilayer alloys," J. Electrochem. Soc. **148**, C620–C626 (2001).
[14] A. Despic and K. Popov, "The effect of pulsating potential on the morphology of metal deposits obtained by mass-transport controlled electrodeposition," J. Appl. Electrochem. **1**, 275–278 (1971).
[15] M. Chandrasekar and M. Pushpavanam, "Pulse and pulse reverse plating—Conceptual, advantages and applications," Electrochim. Acta **53**, 3313–3322 (2008).
[16] A. M. Pesco and H. Y. Cheh, "The current distribution within plated through-holes I. The effect of electrolyte flow restriction during DC electrolysis," J. Electrochem. Soc. **136**, 399–407 (1989).
[17] H. H. Wan, R.-Y. Chang, and W.-L. Yang, "Current distribution in a jet through-hole system during periodic electrolysis," J. Electrochem. Soc. **140**, 1380–1387 (1993).
[18] G. Devaraj, S. Guruviah, and S. Seshadri, "Pulse plating," Mater. Chem. Phys. **25**, 439–461 (1990).
[19] N. Ibl, "Some theoretical aspects of pulse electrolysis," Surf. Technol. **10**, 81–104 (1980).
[20] M. Datta and D. Landolt, "Experimental investigation of mass transport in pulse plating," Surface Technology **25**, 97–110 (1985).
[21] D.-T. Chin, "Mass transfer and current-potential relation in pulse electrolysis," J. Electrochem. Soc. **130**, 1657–1667 (1983).
[22] T. Pearson and J. Dennis, "The effect of pulsed reverse current on the polarization behaviour of acid copper plating solutions containing organic additives," J. Appl. Electrochem. **20**, 196–208 (1990).
[23] C. Kollia, Z. Loizos, and N. Spyrellis, "Influence of pulse reversed current technique on the crystalline orientation and surface morphology of nickel electrodeposits," Surf. Coat. Technol. **45**, 155 (1991).
[24] J. Puippe and N. Ibl, "The morphology of pulse-plated deposits," Plat. Surf. Finish. **67**, 68–72 (1980).
[25] P. Bradley and D. Landolt, "Pulse-plating of copper–cobalt alloys," Electrochim. Acta **45**, 1077–1087 (1999).
[26] C. J. Raub and A. Knödler, "The electrodeposition of gold by pulse plating," Gold Bull. **10**, 38–44 (1977).
[27] D. E. Engelhaupt, "Method of forming electrodeposited anti-reflective surface coatings," U.S. patent 5,326,454 (5 July 1994).
[28] J. Rasmussen, "Making pulse plating work for PCB metallization," Circuitree **17**, 28–30 (2004).
[29] N. Mandich, "Pulse and pulse-reverse electroplating," Metal Finish. **97**, 375–380 (1999).
[30] J. L. Martin, S. Menard, and D. N. Michelen, "Programmed pulse electroplating process," U.S. patent 6,071,398 (6 June 2000).
[31] S. Beattie and J. Dahn, "Single bath, pulsed electrodeposition of copper-tin alloy negative electrodes for lithium-ion batteries," J. Electrochem. Soc. **150**, A894–A898 (2003).
[32] J.-Y. Fei and G. Wilcox, "Electrodeposition of Zn–Co alloys with pulse containing reverse current," Electrochim. Acta **50**, 2693–2698 (2005).
[33] D. L. Grimmett, M. Schwartz, and K. Nobe, "A comparison of DC and pulsed Fe-Ni alloy deposits," J. Electrochem. Soc. **140**, 973–978 (1993).
[34] F.-Y. Shen, W.-P. Dow, A.-H. Liu, J.-Y. Lin, P.-H. Chang, and S.-M. Huang, "Periodic pulse reverse Cu plating for through-hole filling," ECS Electrochem. Lett. **2**, D23–D25 (2013).
[35] C. Toumazou, F. Lidgey, and C. Makris, "Extending voltage-mode op amps to current-mode performance," IEE Proc., Part I: Solid-State Electron Devices **137**, 116–130 (1990).
[36] R. Bragos, J. Rosell, and P. Riu, "A wide-band AC-coupled current source for electrical impedance tomography," Physiol. Meas. **15**, A91 (1994).
[37] P. Bertemes-Filho, B. Brown, and A. Wilson, "A comparison of modified Howland circuits as current generators with current mirror type circuits," Physiol. Meas. **21**, 1 (2000).
[38] F. Seoane, R. Bragós, and K. Lindecrantz, "Current source for multifrequency broadband electrical bioimpedance spectroscopy systems. A novel approach," in *Engineering in Medicine and Biology Society, 2006. EMBS'06. 28th Annual International Conference of the IEEE* (IEEE, 2006), pp. 5121–5125.
[39] H. Hong, M. Rahal, A. Demosthenous, and R. H. Bayford, "Comparison of a new integrated current source with the modified Howland circuit for EIT applications," Physiol. Meas. **30**, 999 (2009).
[40] L. Constantinou, I. F. Triantis, R. Bayford, and A. Demosthenous, "High-power CMOS current driver with accurate transconductance for electrical impedance tomography," IEEE Trans. Biomed. Circuits Syst. **8**, 575–583 (2014).

© Author(s) 2019

[41] D. Bouchaala, O. Kanoun, and N. Derbel, "High accurate and wideband current excitation for bioimpedance health monitoring systems," Measurement **79**, 339–348 (2016).

[42] A. S. Ross, G. Saulnier, J. Newell, and D. Isaacson, "Current source design for electrical impedance tomography," Physiol. Meas. **24**, 509 (2003).

[43] E. Basham, Z. Yang, and W. Liu, "Circuit and coil design for *in-vitro* magnetic neural stimulation systems," IEEE Trans. Bioed. Circuits Syst. **3**, 321–331 (2009).

[44] K. Sooksood, T. Stieglitz, and M. Ortmanns, "An active approach for charge balancing in functional electrical stimulation," IEEE Trans. Biomed. Circuits Syst. **4**, 162–170 (2010).

[45] M. Schuettler, M. Franke, T. B. Krueger, and T. Stieglitz, "A voltage-controlled current source with regulated electrode bias-voltage for safe neural stimulation," J. Neurosci. Methods **171**, 248–252 (2008).

[46] P. Bertemes Filho, "Tissue characterisation using an impedance spectrosopy probe," Ph.D. thesis, University of Sheffield, 2002.

[47] K. R. Aroom, M. T. Harting, C. S. Cox, Jr., R. S. Radharkrishnan, C. Smith, and B. S. Gill, "Bioimpedance analysis: A guide to simple design and implementation," J. Surg. Res. **153**, 23–30 (2009).

[48] D. Chen, X. Deng, and W. Yang, "Comparison of three current sources for single-electrode capacitance measurement," Rev. Sci. Instrum. **81**, 034704 (2010).

[49] P. Bertemes-Filho, A. Felipe, and V. C. Vincence, "High accurate Howland current source: Output constraints analysis," Circuits Syst. **4**, 451 (2013).

[50] D. Sheingold, "Impedance and admittance transformations using operational amplifiers," Lightning Empiricist **12**, 1–8 (1964).

[51] TexasInstruments, "An-1515 a comprehensive study of the Howland current pump," Application Note, 2008, pp. 1–17.

[52] G. Hammond, C. Speake, and M. Stiff, "Noise analysis of a Howland current source," Int. J. Electron. **95**, 351–359 (2008).

[53] S. Fernandez Santos and P. Bertemes-Filho, "Note: Temperature effects in the modified Howland current source for electrical bioimpedance spectroscopy," Rev. Sci. Instrum. **88**, 076103 (2017).

[54] A. Mahnam, H. Yazdanian, and M. M. Samani, "Comprehensive study of Howland circuit with non-ideal components to design high performance current pumps," Measurement **82**, 94–104 (2016).

[55] P. Bertemes-Filho and A. Felipe, "The effect of the random distribution of electronic components in the output characteristics of the Howland current source," J. Phys.: Conf. Ser. **434**, 012019 (2013).

[56] W. Wang, M. Brien, D. Gu, and J. Yang, "A comprehensive study on current source circuits," in *13th International Conference on Electrical Bioimpedance and the 8th Conference on Electrical Impedance Tomography* (Springer, 2007), pp. 213–216.

[57] B. Trump, Power Amplifier Stress and Power Handling Limitations, Burr-Brown, No. AB-039, 1993.

[58] P. J. Smith and D. H. Shin, *Inkjet-Based Micromanufacturing* (John Wiley and Sons, 2012).

[59] See https://www.lopec.com/ for information about the market of printed electronics; accessed 20 January 2019.

[60] J. Perelaer, A. W. De Laat, C. E. Hendriks, and U. S. Schubert, "Inkjet-printed silver tracks: Low temperature curing and thermal stability investigation," J. Mater. Chem. **18**, 3209–3215 (2008).

[61] J. Perelaer, P. J. Smith, D. Mager, D. Soltman, S. K. Volkman, V. Subramanian, J. G. Korvink, and U. S. Schubert, "Printed electronics: The challenges involved in printing devices, interconnects, and contacts based on inorganic materials," J. Mater. Chem. **20**, 8446–8453 (2010).

[62] D. Mager, A. Peter, L. Del Tin, E. Fischer, P. J. Smith, J. Hennig, and J. G. Korvink, "An mri receiver coil produced by inkjet printing directly on to a flexible substrate," IEEE Trans. Med. Imaging **29**, 482–487 (2010).

[63] F. Molina-Lopez, D. Briand, and N. De Rooij, "All additive inkjet printed humidity sensors on plastic substrate," Sens. Actuators, B **166**, 212–222 (2012).

[64] N. Wang, M. Meissner, N. MacKinnon, V. Luchnikov, D. Mager, and J. Korvink, "Fast prototyping of microtubes with embedded sensing elements made possible with an inkjet printing and rolling process," J. Micromech. Microeng. **28**, 025003 (2017).

[65] B. Warren, "X-ray diffraction in random layer lattices," Phys. Rev. **59**, 693 (1941).

© Author(s) 2019